Available online at www.sciencedirect.com

ScienceDirect

Underground Space 24 (2025) 180–196

www.keaipublishing.com/undsp

Research Paper

Impact of ground motion characteristics on the seismic fragility of circular tunnels

Zhong-Kai Huang [a], Dong-Mei Zhang [a,b,*], Wu-Yu Zhang [b], Yong-Bo Li [c]

[a] Department of Geotechnical Engineering, Tongji University, Shanghai 200092, China
[b] College of Civil Engineering and Water Resources, Qinghai University, Qinghai 810016, China
[c] CCCC Tunnel Engineering Bureau Co., Ltd., Shanghai 200332, China

Received 2 June 2023; received in revised form 19 September 2024; accepted 26 September 2024
Available online 9 July 2025

Abstract

The seismic performance of tunnel structure can be examined by fragility analysis, which determines the probability that demand will exceed capacity for a given hazard intensity. Although it is commonly understood that earthquake uncertainties dominate fragility features, the implication of ground motion characteristics on the shield tunnel fragility analysis has not been comprehensively explored. Thus, this study aims to compare the effects of various earthquake characteristics on the fragility of the investigated shield tunnels. To this end, a typical shield tunnel was chosen and modelled using the finite element software. In addition, to account for typical ground motion characteristics, various ground motion sets, including near-field no plus motions (NFNP), near-field motions with a pulse (NFP), and far-field motions (FF), are selected, and a fragility analysis was assessed for every set of ground motion. The fragility curves were generated employing peak ground acceleration (PGA) as the intensity measure (IM) and tunnel drift as the damage measure (DM). The findings indicate that shield tunnels subjected to NFP may be more vulnerable compared to those subjected to NFNP and FF ground motions. This study's findings highlight the vital role of ground motion characteristics in evaluating the fragility of shield tunnels. Moreover, the results may inform future seismic risk and resiliency evaluations regarding the importance of considering or disregarding the impacts of ground motion characteristics on tunnel vulnerability.

Keywords: Ground motion characteristics; Shield tunnel; Seismic vulnerability; Resilience assessment

1 Introduction

Tunnels are one of the most common underground structures in contemporary urban cities (Patil et al., 2018; Chen et al., 2023). These infrastructures are susceptible to damage from high-level seismic activity (Hashash et al., 2005; Li et al., 2025). For instance, it was reported that more than 10% of the tunnels in the area near the epicentre suffered significant damage as a result of the 1995 Hyogoken-Nambu earthquake (Asakura & Sato, 1996). Two other notable examples of tunnel collapse are the Bolu tunnel in Turkey, which sustained damage and failed after the 1999 Kocaeli earthquake (Kontoe et al., 2008), and the Longxi tunnel in China, which suffered significant damage during the 2008 Wenchuan earthquake (Li, 2012). Consequently, it is imperative to conduct a thorough study of the earthquake risk of tunnels. A key element of risk assessment is seismic vulnerability analysis, which is frequently used to determine the possibility that the structure under examination may sustain a specific degree of damage at a given earthquake intensity (Kassem et al., 2020).

An enormous amount of work has gone into creating seismic fragility curves for tunnels, taking into account various factors such as tunnel typologies, damage states, soil conditions, intensity measures, and uncertainty factors. In

* Corresponding author at: Department of Geotechnical Engineering, Tongji University, Shanghai 200092, China.
E-mail address: dmzhang@tongji.edu.cn (D.-M. Zhang).
Peer review under the responsibility of Tongji University

https://doi.org/10.1016/j.undsp.2024.09.008

the past two decades, expert judgment approach (Dowding & Rozan, 1978) and earthquake damage investigation method (American Lifelines Alliance (ALA), 2001) have been commonly used for seismic vulnerability analysis of tunnels due to their simplicity. However, relying on expert judgment and limited earthquake damage data can lead to major misestimation of tunnel vulnerability (Tsinidis et al., 2022). Thanks to advancements in computing power, numerical approaches for seismic vulnerability analysis of tunnels have been developed and applied worldwide. For example, Argyroudis and Pitilakis (2012) established fragility functions of shallow-buried tunnels considering different site conditions and structural sizes. Fabozzi et al. (2017) and Qiu et al. (2018) proposed fragility curves for horseshoe-shaped rock tunnels using the incremental dynamic analysis method. Andreotti and Lai (2019) developed fragility functions of rock tunnels and suggested optimal design for initial and secondary lining thicknesses. Hu et al. (2020) used a similar methodology to investigate the impact of various soil layers, soil-structure interaction and tunnel burial depth, on the seismic fragility of tunnels. Huang et al. (2021) investigated the optimal earthquake intensity measures (IMs) for shield tunnels in Shanghai City and proposed the corresponding fragility curves. The study demonstrated that peak ground acceleration (PGA) and peak ground velocity (PGV) were the optimal IMs for shallow-buried and deep-buried shield tunnels, respectively. Based on vector IMs, Huang and Zhang (2021) proposed the seismic fragility surfaces for shield tunnels and showed the importance of tunnel burial depths in the seismic vulnerability. de Silva et al. (2021) established a set of fragility curves of tunnels constructed in sandy site, and verified them with existing empirical curves. Some researchers also investigated the aging effects on the tunnel fragility. Argyroudis et al. (2017) investigated the effect of reinforcement material corrosion deterioration on the evolution of seismic fragility of tunnels. Huang et al. (2022) proposed time-dependent fragility analysis framework for tunnels with different burial depths in soft soil area. The fragility of existing shield tunnels was further analyzed by Liu et al. (2022), with particular attention given to the influence of surface high-rise buildings and tunnel bolt corrosion. Machine learning methods, such as support vector machines (Huang et al., 2017), artificial neural networks (Huang & Chen, 2022), and the random forest algorithm (Wang et al., 2023), have also been utilized by some scholars to improve the efficiency of seismic fragility assessment for tunnels. More recently, some researchers also examined the effects of ground-tunnel relative flexibility (Tsinidis et al., 2024), spatial variation of site shear-wave velocity (Zhong et al., 2023), and mainshock–aftershock ground motion sequences (Zhong et al., 2024) on the tunnel seismic fragility.

Although the above references provide ample study on the seismic fragility of tunnels under various conditions such as burial depth, lining thickness, soil properties, and lining material degradation, neglecting the ground motion characteristics may lead to overestimation or underestimation of the seismic fragility of tunnels. The earthquake intensity and frequency content of the seismic records may pose a crucial impact on the dynamic behavior of circular tunnels. Currently, comprehensive investigations regarding the implications of ground motion characteristics on the seismic fragility analysis of shield tunnels are lacking. Thus, this paper employs a large numbers of nonlinear seismic response analyses on tunnels considering typical ground motion characteristics of different sets, including near-field no plus motions (NFNP), near-field motions with a pulse (NFP), and far-field motions (FF). This paper proposes seismic fragility curves for the examined circular tunnels and highlights the influences of various ground motion features on their seismic vulnerability. The suggested fragility curves are ultimately evaluated with the empirical ones found in the literature, so as to provide a systematic examination and discussion of the differences.

2 Methodology

The adopted procedure to create the fragility curves of the tunnels under investigation is displayed in Fig. 1, which involves a total of six steps summarized in the following sections:

Step 1 encompasses the presentation of the basic definition of the examined soil-tunnel configuration. This includes information regarding the geometry, material, burial depth of the examined tunnels, as well as the stiffness and damping characteristics of the adopted soil profiles.

Step 2 illustrates the selection of earthquake records and the IM employed in the numerical simulations.

Step 3 involves the construction of a numerical model using the soil-tunnel configuration presented in Step 1 and the input earthquakes from Step 2.

Step 4 outlines the adopted DM utilized for evaluating the condition of the examined tunnels. Additionally, it describes the corresponding limit states and thresholds associated with different damage states.

Step 5 focuses on the analysis of the DM evolution with the IM according to numerous numerical analyses. The computation of the uncertainty in demand (β_{D}), and the determination of mean values and standard deviation for the lognormal probability distribution function, is carried out in this step. These parameters play a crucial role in defining the fragility curves.

Step 6 is dedicated to deriving the fragility curves for the examined tunnels, utilizing the adopted IM and the parameters obtained in Step 5. Typically, a lognormal cumulative distribution function can be employed to analytically express the fragility curves (Nielson & DesRoches, 2007; Moschonas et al., 2009). The formulation is as follows:

$$P[D_{\mathrm{S}} \geq D_{\mathrm{S},i} \mid \mathrm{IM}] = \Phi\left(\frac{\ln \mathrm{IM} - \ln \mathrm{IM}_{\mathrm{DS},i}}{\beta_{\mathrm{tot}}}\right), \tag{1}$$

where P represents the conditional likelihood that a specific damage state ($D_{\mathrm{S},i}$) will occur under a particular earth-

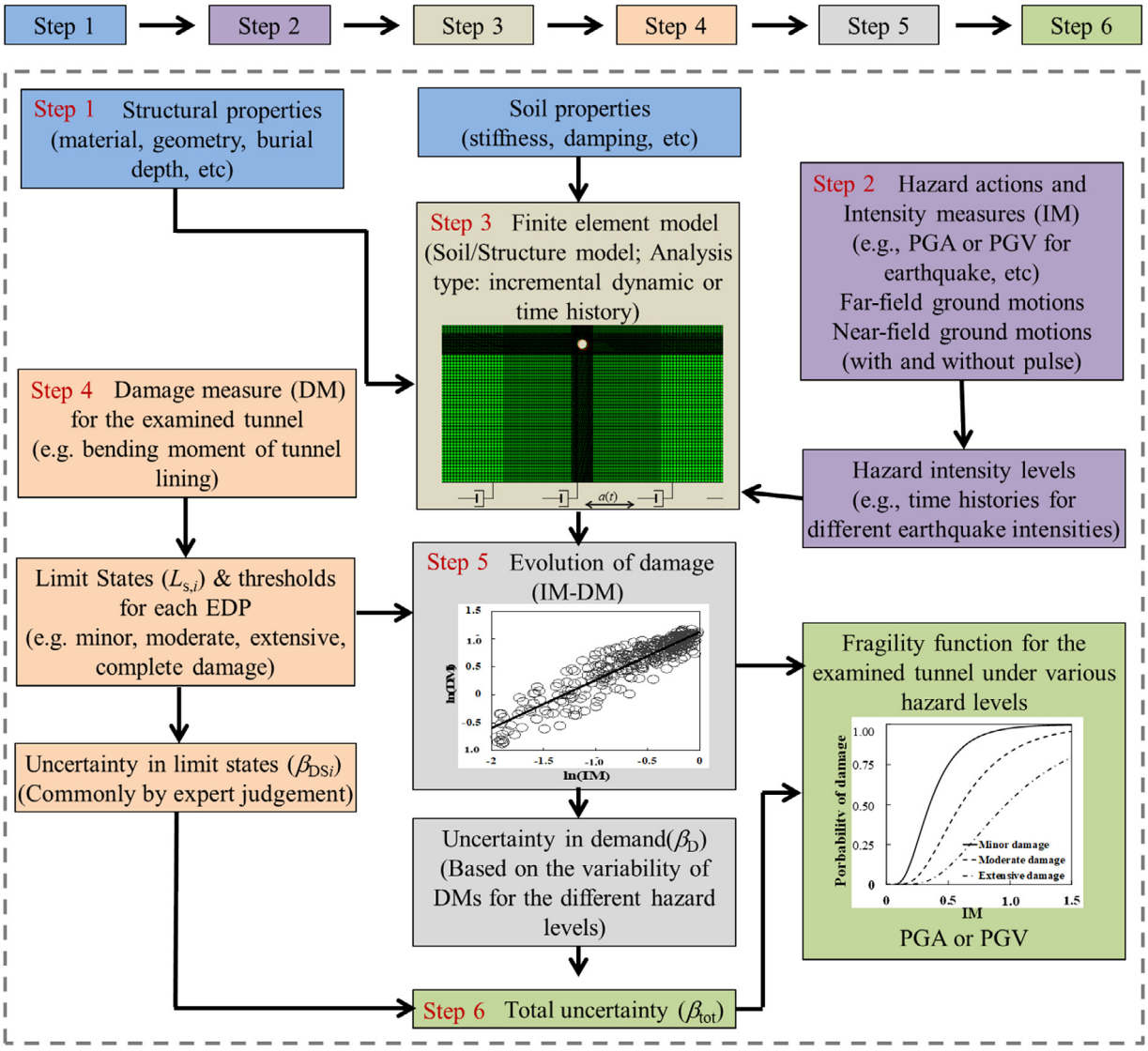

Fig. 1. Basic procedure for the generation of the seismic fragility functions for the examined tunnels.

quake intensity measure (IM); D_S denotes the damage state of tunnel lining; the cumulative distribution function of the standard normal distribution is represented by Φ and the median threshold value of IM that results in a particular $D_{S,i}$ is denoted by $IM_{DS,i}$. The term β_{tot} refers to the total standard deviation of the lognormal distribution, indicating the overall variation associated with every damage state. This can be further calculated using the following formula:

$$\beta_{tot} = \sqrt{\beta_{DSi}^2 + \beta_D^2}\ . \tag{2}$$

Here, β_{DSi} is determined as the lognormal standard deviations of the damage state thresholds. The uncertainty resulting from the seismic demand is represented by β_D, which can be expressed as the variability of the simulated DMs compared to the regression fit. It is worth highlighting that the specific values of β_{DSi} will be provided in Section 3.4. An illustrative example demonstrating the derivation of β_D and β_{tot} is presented in Fig. 2. The 'Log std' in Fig. 2 means the standard deviation of the lognormal distribution. The analysis results given in the form of DM across various earthquake severity levels are represented by the various data points on the graph. Regression analysis is used to construct the solid line, and the average threshold value of the intensity measure (IM_{mi})) needed to induce the ith damage state ($D_{S,i}$) is determined according to how the DM defines this damage state.

3 Numerical case study

The studied tunnel has a lining with a thickness of 0.35 m and an external diameter of 6.2 m. It is immersed at a depth of 15.0 m. The tunnel is built in a clayey soil profile that reaches a depth of 70 m and is supported by elastic bedrock. Figure 3(a) depicts the clayey soil profile that was taken into consideration, which is associated with soil type C by the EuroCode 8 (EC8, 2004). It is evident that there

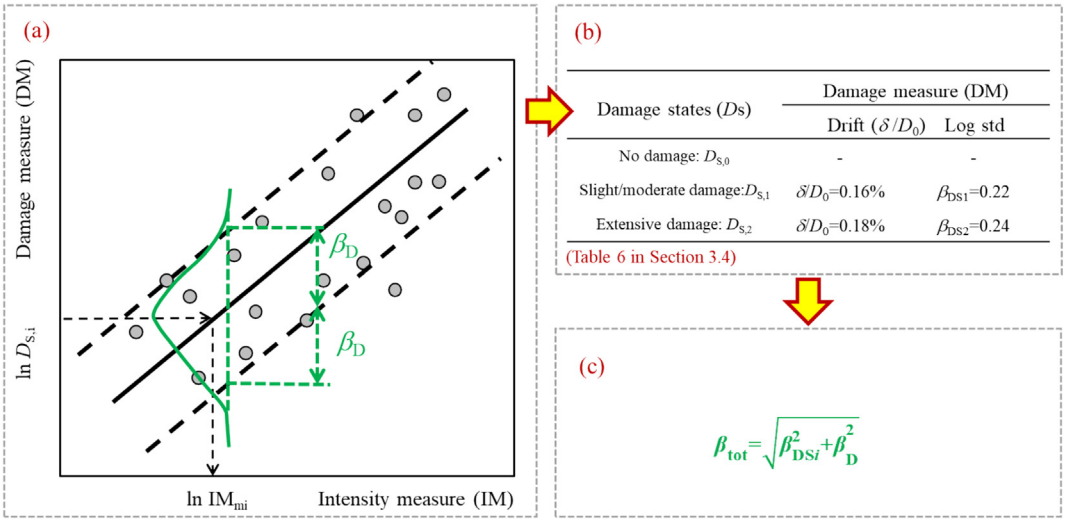

Fig. 2. An illustration of how to derive β_D and β_{tot} from the progression of damage using intensity measure (IM). (a) Determination of β_D, (b) determination of β_{DSi}, and (c) determination of β_{tot} based on β_D and β_{DSi}.

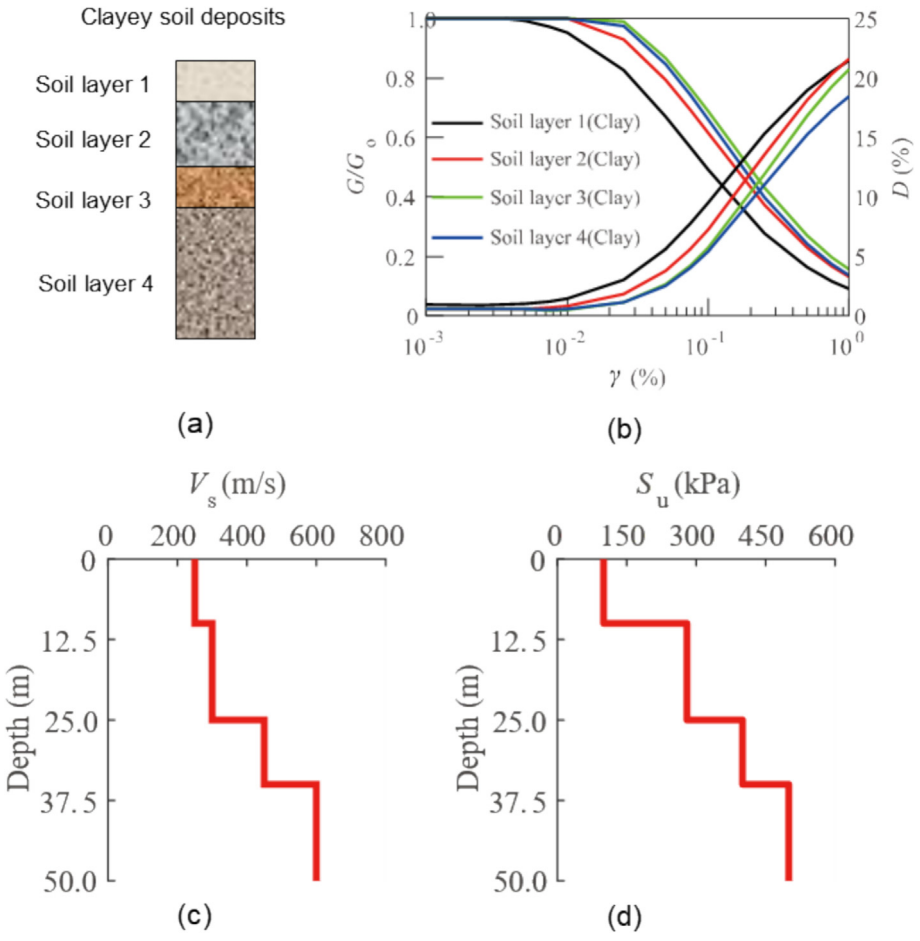

Fig. 3. (a) Soil profile, (b) adopted G-γ-D curves (Ishibashi & Zhang, 1993), (c) undrained shear strength (S_u), and (d) small strain shear wave velocity (V_s).

are four distinct soil layers. Layers 1 and 2 are composed of soft soils that are clayey, whilst layers 3 and 4 consist of typical stiff clayey soils. The density of the uppermost two layers is 1.8 t/m^3, but the density of the lowermost two layers is 1.9 t/m^3. The Poisson's ratio across each soil layer is consistently set at 0.40. Figure 3(b) and (c) illus-

trates the variation of the undrained shear strength (S_u) and shear wave velocity (V_s) throughout different soil layers.

The G-γ-D curves provided by Ishibashi and Zhang (1993) were utilized to characterize the nonlinear seismic pattern of the analyzed soil deposit shown in Fig. 3(d). Within the given figure, the notation defines G as the shear modulus of soil, γ as the shear strain, and D as the damping ratio. Four ensembles of G-γ-D curves were used to calibrate the important parameters of the soil constitutive model. These parameters are offered in the next part. The elastic bedrock has a shear wave velocity of 1000 m/s and a density of 2.2 t/m^3.

3.1 Finite element model

The numerical model is created using the commercial computational finite element (FE) program ABAQUS (ABAQUS, 2012), using the information given about the soil profile and tunnel. Figure 4 illustrates the standard configuration of the FE model. The H and d in Fig. 4 represent the burial depth and the tunnel diameter. The length of the FE model is established as 200 m in order to investigate the potential influence of the boundaries on the structural response of the investigated tunnel, as determined by the sensitivity assessment. The depth of the numerical model corresponds to the depth of the chosen soil layers.

The soil region is discretized using plane strain elements (CPE4) to facilitate accurate wave propagation and cover the entire range of frequencies important to the analysis (i.e., 0.5–10 Hz). The dimensions of the soil element are precisely adjusted to be in close proximity to the tunnel lining, which is modeled using beam elements (B21). A face-to-face contact (ABAQUS, 2012) is used to simulate the interaction regarding the tunnel lining and soil. The interface's normal direction utilizes a rigid contact, while its tangential direction employs a coulomb friction model with a friction coefficient of 0.4. The soil damping coefficient is consistently set to 5% for all soil layers to accurately represent the viscous damping at low levels of deformation. This damping is mathematically represented using the Rayleigh form, as outlined in the approach established by Hashash et al. (2001). The seismic response evaluations undertaken by different researchers such as Ganainy and Naggar (2009) and Lou and Shao (2013), reveal significant variation in the selection of viscous damping values for soil. This study adheres to prevailing methodologies by employing the commonly employed 5% damping coefficient for the examined soil strata, in accordance with recent investigations conducted by Huang et al. (2017), He and Chen (2019), and Zi et al. (2021). This range is regarded as indicative of actual soil damping values during vigorous ground movements. Future investigations will aim to ascertain a more precise and accurate soil damping coefficient for the particular soil-tunnel scenario.

Ensuring the accuracy of the seismic behavior of the soil-tunnel system relies heavily on the proper specification of the boundary constraints in the numerical model. The vertical boundary of the numerical model was defined by imposing kinematic tie restrictions on the two nodes of the side boundaries, ensuring that they have equal elevations relative to the bedrock. The horizontal displacement pattern is symmetrical on both sides of the FE model. Furthermore, dashpots are placed along the base of the numerical model, in accordance with the approach established via Lysmer and Kuhlemeyer (1969). The coefficient of the dashpots can be calculated by multiplying the shear wave velocity and the density of the underlying bedrock, and then multiplying it by the equivalent 'soil' surface, denoted as S. This ensures that the findings remain proportional for any horizontal element size. Specifically, the base boundary was subjected to shaking ground motions through the implementation of dashpots, utilizing acceleration time histories. The analyses were conducted by scaling these records to various magnitudes of PGA under outcropping conditions. This modeling approach has been demonstrated to be reasonably accurate and has been employed in prior research by Argyroudis et al. (2017), Jiang et al. (2022), Tsinidis et al. (2022), and others.

The seismic performance of tunnel structures in clayey soils under earthquake loading is commonly modeled

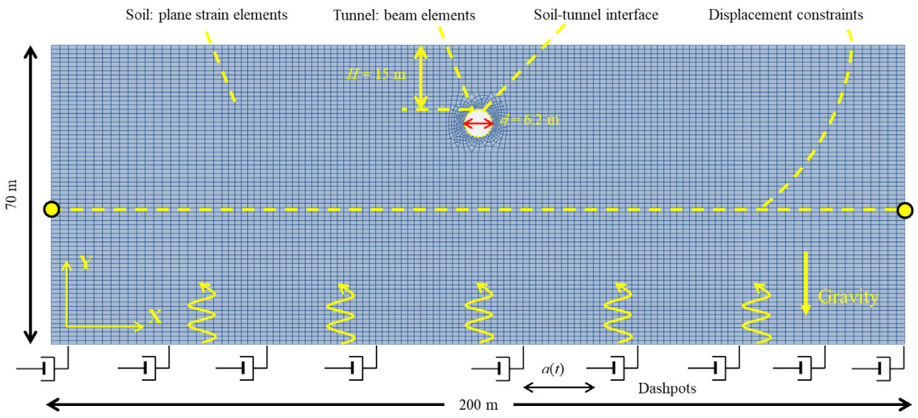

Fig. 4. Numerical model of the soil-tunnel system.

under undrained conditions using total stress numerical simulations. In order to account for the initial geostress in the FE model, a geostatic step is introduced, where the base of the model is fixed in both the vertical and horizontal directions. Afterwards, the application of seismic loading occurs in an implicit dynamic analysis stage. Ultimately, the model base is allowed to move horizontally without any restrictions, and artificial ground motions are applied using horizontal dashpots to assess the seismic behavior of the tunnels.

3.2 Material constitutive model and parameters

3.2.1 Modelling of the soil behavior: non-linear kinematic hardening model

This study utilized the non-linear kinematic hardening (KH) model (Anastasopoulos et al., 2010, 2011; Bilotta et al., 2014; Wu et al., 2020) to predict the dynamic behavior of soil under earthquake loading. The KH model, employed in this study, has effectively elucidated the dynamic characteristics of clay under undrained conditions in prior investigations (Tsinidis, 2018; Al-Janabi & Aubeny, 2022). The KH model's evolution law incorporates both an isotropic and a nonlinear kinematic hardening component. The isotropic component determines the variation of the equivalent stress, while the nonlinear kinematic hardening component governs the translation of the yield surface. The kinematic hardening component consists of a kinematic term and a relaxation term that takes into consideration the nonlinear properties.

The general evolution of stresses (σ) is detailed as follows (Anastasopoulos et al., 2011):

$$\sigma = \sigma_0 + \alpha, \tag{3}$$

where σ_0 signifies the zero plastic strain stress, and α represents the stress related to the kinematic development of the yield surface in the stress space (backstress). The expression that defines the yield surface (F) is as follows:

$$F = f(\sigma - \alpha) - \sigma_0, \tag{4}$$

where $f(\sigma - \alpha)$ represents the Mises stress that is identical to the backstress. The plastic flow rate, $\dot{\varepsilon}^{pl}$, is defined in accordance with the plastic flow rule as follows:

$$\dot{\varepsilon}^{pl} = \dot{\bar{\varepsilon}}^{pl} \frac{\partial F}{\partial \sigma}, \tag{5}$$

where $\dot{\varepsilon}^{pl}$ denotes the plastic flow rate, and $\dot{\bar{\varepsilon}}^{pl}$ represents the equivalent rate of plastic strain.

The model's evolutionary framework includes an isotropic hardening component that characterizes the alteration in equivalent stress, determining the dimensions of the yield surface σ_0 based on plastic deformation. In addition, a non-linear kinematic hardening component explains the movement of the yield surface in the stress space. The latter is defined as a combination of a kinematic component and a relaxation component, which introduces a subtle level of nonlinearity.

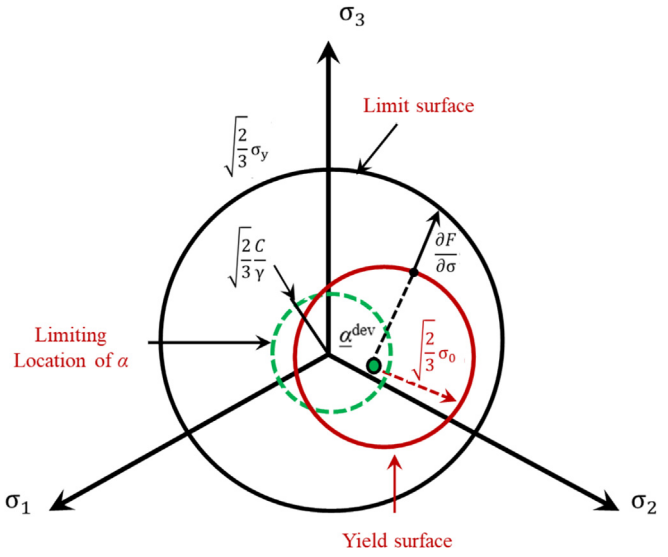

Fig. 5. Three-dimensional illustration of the hardening law for a nonlinear isotropic/kinematic hardening constitutive soil model.

Figure 5 demonstrates the progressive changes in the two types of hardening components (isotropic and kinematic) when subjected to both unidirectional and multiaxial loading situations. The governing principle of the kinematic hardening component states that the backstress α is contained inside a cylindrical domain with a radius equal to $\sqrt{2/3}C/\gamma$ (where C represents initial kinematic hardening modulus). The yield surface is bounded, meaning that every stress point must be located within a cylindrical region with a radius of $\sqrt{2/3}\sigma_y$. Here, σ_y represents the highest yield stress at saturation, especially when there are significant plastic strains.

The isotropic hardening component σ_s of the yield stress is particularly defined by the growth of the yield surface size and may be accurately expressed using the simplified exponential method, as stated below:

$$\sigma_s = \sigma_0 + M_\infty \left(1 - e^{-b\bar{\varepsilon}^{pl}}\right), \tag{6}$$

where σ_0 indicates the yield stress when there is no plastic strain, M_∞ refers to the model coefficients that represents the maximum variation in the size of the yield surface, b represents the rate of change with the development of plastic strain, and $\bar{\varepsilon}^{pl}$ represents the equivalent plastic strain.

The following expression could be adopted to describe the kinematic hardening component of the yield stress (Anastasopoulos et al., 2010):

$$\dot{\alpha} = E_s \frac{1}{\sigma_0}(\sigma - \alpha)\dot{\bar{\varepsilon}}^{pl} - \theta\alpha\dot{\bar{\varepsilon}}^{pl}, \tag{7}$$

where E_s represents the soil's initial kinematic hardening modulus, which is equal to its small-strain elastic stiffness; θ reflects the drop rate of the kinematic hardening as the plastic deformation increases. Here, the value of θ for the clay being studied is determined employing the subsequent equation:

$$\theta = E_S/[\sqrt{3}S_u - \sigma_0]. \quad (8)$$

The KH model could be characterized by three key parameters: the ultimate strength σ_y, the elastic Young's modulus E_S, and the yield stress σ_0 of the soil, as indicated by Eqs. (3)–(8). The parameter σ_0 determines the onset of nonlinear behavior, specifically the soil's yield stress at zero plastic strain. This can be further defined as a percentage λ of the yield stress σ_y, i.e., $\sigma_0 = \lambda \times \sigma_y$.

Physical model tests conducted on piles (Kanellopoulos & Gazetas, 2020), underground stations (Wu et al., 2020), tunnel structures (Antoniou et al., 2023), and retaining walls (Anastasopoulos et al., 2010), among other research objects, were effective in validating the KH model. The study utilized numerical analysis to conduct cyclic simple shear tests in order to precisely calibrate the coefficient λ of the four clayey soil layers being studied, as described by Anastasopoulos et al. (2010). The values of λ were computed to vary from 1/4 to 1/25 for the examined four soil layers. The KH model is calibrated using the 'target' G-γ-D curves shown in Fig. 6(a) and (b) for soil layers 1 and 2, respectively. Figure 6(c) and (d) depicts the stress–strain loops for soil layers 1 and 2, respectively, which have been derived by numerical simulation.

3.2.2 Modelling of the tunnel lining: concrete damaged plasticity model

The Lee and Fenves (1998) concrete damage plasticity model was employed to simulate the nonlinear response of tunnel lining concrete. The model integrates the notion of concrete fracture energy and accounts for two common failure mechanisms of the concrete material, specifically tensile cracking and compressive crushing, as depicted in Fig. 7 (ABAQUS, 2012), when subjected to uniaxial tension and compression stresses. The elastic stiffness degradation of the concrete material during tension and compression is described in terms of two damage variables, d_t and d_c, and the model's yield function is modified by multiple hardening variables (Lee & Fenves, 1998). The present study employed concrete type C45, with Tables 1 and 2 presenting the two dynamic concrete damage parameters under uniaxial loading. Tensile fracture damage is observed as the tensile damage factor d_t exceeds 0, while concrete cracking is detected when the compression damage factor d_c exceeds 1. The concrete material is damaged during compression when d_c is greater than 0.

3.3 Adopted seismic records

To study the influences of ground motion characteristics on the fragility analysis of the examined tunnel structures, three distinct types of ground motion were selected thorough the Pacific Earthquake Engineering Research Strong Motion Database (2000). The selected ground motion packages consist of NFNP, NFP, and FF, as described in Tables 3–5. As can be seen in Table 3–5, the NFNP and the NFP have a lower source-to-site distance than the FF. Moreover, the pulse effects are disregarded

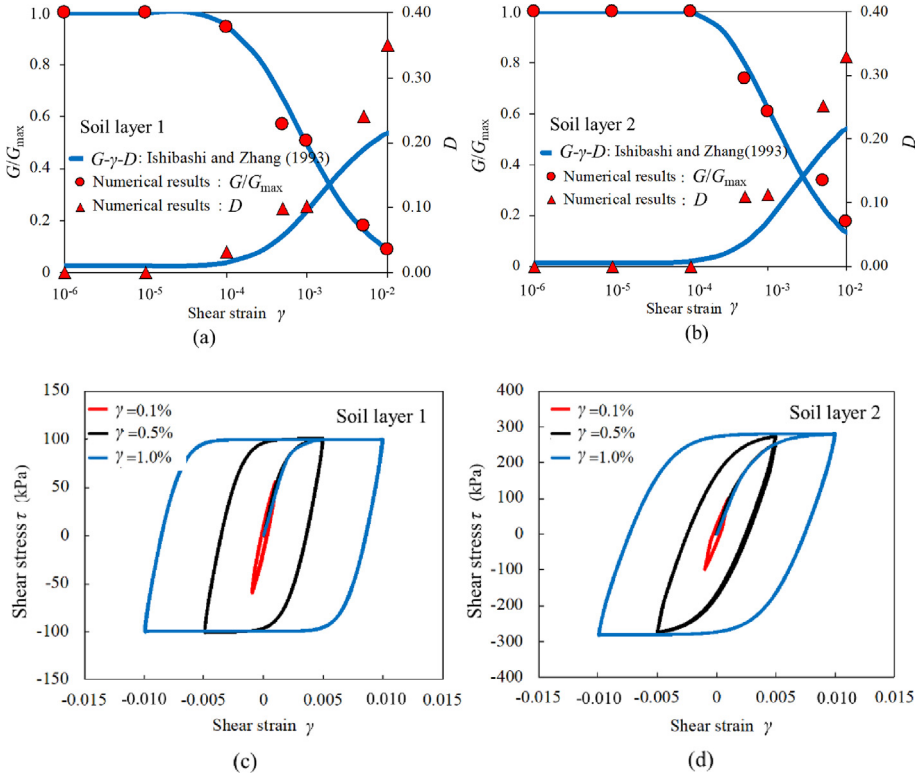

Fig. 6. Calibration of constitutive parameters for the KH model using the 'target' G-γ-D curves for (a) soil layer 1 and (b) soil layer 2; typical stress–strain loops for (c) soil layer 1 and (d) soil layer 2 obtained using numerical modelling of cyclic simple shear tests.

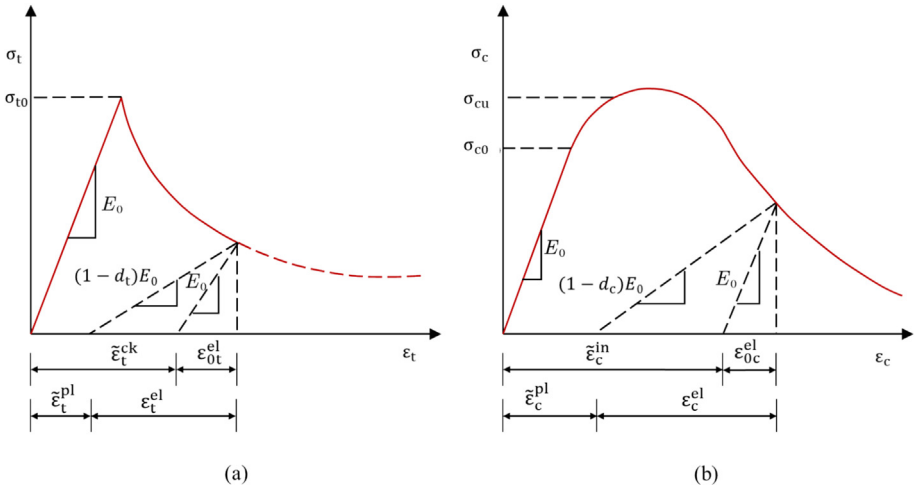

Fig. 7. Nonlinear performance of the concrete under uniaxial loading with regard to (a) tension and (b) compression (ABAQUS, 2012).

Table 1
Tensile damage parameters of the concrete damage plasticity model.

Concrete tension stiffening		Concrete tension damage	
Stress (MPa)	Cracking strain	d_t	Cracking strain
2.51	0	0	0
2.09	0.000 08	0.111	0.000 08
1.38	0.000 16	0.279	0.000 16
0.81	0.000 30	0.552	0.000 30
0.47	0.000 55	0.796	0.000 55
0.32	0.000 89	0.905	0.000 89
0.22	0.001 39	0.955	0.001 39
0.17	0.001 99	0.975	0.001 99
0.14	0.002 59	0.984	0.002 59
0.13	0.002 99	0.988	0.002 99
0.09	0.004 98	0.990	0.004 98

Table 2
Compressive damage parameters of the concrete damage plasticity model.

Concrete compression stiffening		Concrete compression damage	
Stress (MPa)	Cracking strain	d_c	Cracking strain
14.35	0	0	0
28.08	0.000 36	0.116	0.000 36
29.64	0.000 76	0.208	0.000 76
24.72	0.001 66	0.405	0.001 66
14.31	0.003 47	0.711	0.003 47
10.42	0.004 68	0.820	0.004 68
7.49	0.006 26	0.895	0.006 26
5.80	0.007 80	0.932	0.007 80
4.72	0.009 31	0.953	0.009 31
3.98	0.010 82	0.965	0.010 82
3.15	0.013 32	0.977	0.013 32
2.35	0.017 28	0.987	0.017 28

in the NFNP while taken into account in the NFP. The set of NFNP records consists of 12 distinct records with a PGA ranged from 0.12g to 0.58g, the set of NFP records consists of 12 distinct components with a PGA varied from 0.23g to 0.83g, and the set of FF records consists of 24 distinct components with a PGA varied from 0.11g to 0.73g. The initial ground motion suites' spectral acceleration responses, as well as their median spectra, are shown in Fig. 8.

Note that the earthquake force input at the bedrock interface was included in the numerical model utilized in this study. Accordingly, the acceleration record observed at the site surface was deconvolved using the DEEPSOIL Software (Hashash et al., 2018) to obtain the bedrock ground motions, as depicted in Fig. 9. Subsequently, the seismic performance of the tunnel structure under a rising level of earthquake intensity was captured by scaling the deconvolved accelerations in steps of 0.1g from 0.1g up to 1.0g.

3.4 Selection of damage measure

The seismic fragility functions can be derived by establishing a regression relationship between DM and the related earthquake IM. The choice of DM is a critical factor in the fragility evaluation of the examined tunnels (Omranian et al., 2018; Kazemi et al., 2023). While various DMs have been proposed for the fragility assessment of critical urban life engineering components, such as bridges, pipelines, dams, and high-rise buildings, the number of DMs available for shield tunnels is still limited (Jiang et al., 2022; Ansari et al., 2023). In this paper, we adopt the DM proposed by Andreotti and Lai (2019) in terms of the tunnel deformation failure criterion. This DM is described using the fraction of the relative displacement (denoted as δ) of the tunnel crown and tunnel invert over the initial diameter (denoted as D_0) of tunnels, as displayed in Fig. 10. To describe the performance of the examined shield tunnel, we introduce a set of three different damage states (Andreotti & Lai, 2019; Sun et al., 2020; Tsinidis et al., 2022), namely no damage, slight/moderate damage, and extensive damage, and display the associated thresholds of the tunnel damage states for various damage levels

Table 3
Selected near-field no-plus ground motions.

No.	Earthquake event	Years	Station	Component	Magnitude M	Source-to-site distance R (km)	PGA (g)
1	Helena_Montana-01	1935	Carroll College	RSN1_HELENA.A_A-HMC180.AT2	6.00	2.07	0.14
2	Parkfield	1966	Cholame – Shandon Array #5	RSN30_PARKF_C05085.AT2	6.19	9.58	0.15
3	Managua_Nicaragua-01	1972	Managua_ESSO	RSN95_MANAGUA_A-ESO090.AT2	6.24	3.51	0.36
4	Parkfield-02_CA	2004	PARKFIELD – GOLD HILL	RSN4067_PARK2004_GOLD-90.AT2	6.00	2.35	0.14
5	Morgan Hill	1984	Anderson Dam (Downstream)	RSN448_MORGAN_AND250.AT2	6.19	3.22	0.41
6	Chalfant Valley-02	1986	Zack Brothers Ranch	RSN558_CHALFANT.A_A-ZAK270.AT2	6.19	6.44	0.44
7	Morgan Hill	1984	Halls Valley	RSN461_MORGAN_HVR150.AT2	6.19	3.45	0.16
8	Duzce	1999	Lamont 1062	RSN1615_DUZCE_1062-N.AT2	7.14	9.14	0.25
9	Tottori	2000	SMNH01	RSN3947_TOTTORI_SMNH01NS.AT2	6.61	5.83	0.58
10	Duzce	1999	Lamont 1059	RSN1612_DUZCE_1059-N.AT2	7.14	4.17	0.12
11	Tottori	2000	SMN015	RSN3943_TOTTORI_SMN015NS.AT2	6.61	9.10	0.27
12	Parkfield-02_CA	2004	PARKFIELD – DONNA LEE	RSN4064_PARK2004_DONNA-90.AT2	6.00	4.25	0.29

in Table 6. This DM was also widely adopted by other scholars in comparable works (e.g., Sun et al., 2020; Tsinidis et al., 2022). It is noted that the difference in normalized drift from slight/moderate damage to extensive damage is relatively small, posing a potential impact on the ultimate seismic fragility results. To address this, further numerical simulations and experimental analysis will be conducted to enhance the comprehension of the dynamic behavior of tunnels subjected to seismic excitations. This comprehensive investigation aims to establish more nuanced and well-founded criteria for the classification of damage states, thereby enhancing both the scientific rigor and practical applicability of seismic fragility analysis.

4 Seismic vulnerability analysis

As discussed in Section 2, a two-parameter fragility model utilizing the logarithm of the mean IM value IM_{mi} and the standard deviation β_{tot} has been selected to characterize the seismic vulnerability of the tunnels under investigation. In contemporary seismic fragility analysis literature, three primary methodologies are notable for describing the correlation between seismic DM and IM. These approaches include incremental dynamic analysis (Vamvatsikos & Cornell, 2002), multiple-stripe analysis (Jalayer & Cornell, 2009), and Cloud analysis (Shome et al., 1998; Huang et al., 2025). The Cloud approach distinguishes itself from model superposition analysis and incremental dynamic analysis because to its high efficiency, which can be attributed to the straightforward foundational formulas it employs, particularly the constant dispersion and linear connection. The Cloud method is able to achieve its goals with a minimal amount of unscaled ground motions. These ground motions are evenly dispersed over different intensity levels of the IM. This approach is used to create probabilistic seismic demand models, also known as DM–IM relationships. These models are used as the foundation for establishing fragility functions. The efficiency of the Cloud technique is apparent in its reliance on a small number of nonlinear dynamic studies using unscaled ground motions, making it a popular option for seismic vulnerability evaluations. Therefore, this study utilizes the Cloud approach to calculate these two pivotal parameters.

The dependent and independent variables in a linear regression analysis on a logarithmic scale are the tunnel DM and the IM (i.e., PGA calculated at the ground surface), respectively. By utilizing the aforementioned regression model of the outcomes of the nonlinear numerical analysis and the damage states criteria presented in Table 6, the mean IM value IM_{mi} that corresponds to the various damage states can be determined. The total standard deviation β_{tot} can be obtained by applying regression analysis using Eq. (2) in Section 2.

4.1 Relationship between DM and IM

The tunnels' damage measure datasets were developed by carrying out nonlinear dynamic simulations to analyze the seismic response of the tunnel structure under various ground motion sets. Figure 11 illustrates the changes in the DM as the IM, specifically the PGA at the surface, increases. These figures represent the NFNP, NFP, FF, and the combined motion sets (All), respectively. It is noted that PGA is adopted as the IM in this paper, supported by its established optimality for generating fragility curves in the context of the analyzed soil-tunnel configuration, as demonstrated in prior research by the authors (Huang et al., 2021). Moreover, it is important to highlight that PGA stands out as the predominant intensity measure in the development of fragility curves for tunnel structures, as evidenced in various studies (e.g., Argyroudis & Pitilakis, 2012; Argyroudis et al., 2017; Qiu et al., 2018).

The red solid line in these figures represents the linear regression fit curve for the data of DM acquired from the numerous nonlinear numerical simulations. The various data points in the figures correspond to the DM values with

Table 4
Selected near-field pulse-like ground motions.

No.	Earthquake event	Years	Station	Component	Magnitude M	Source-to-site distance R (km)	PGA (g)
1	Imperial Valley-06	1979	EI Centro Array #4	IMPVALL.H/H-E04140	6.53	7.05	0.48
2	Imperial Valley-06	1979	EI Centro Array #7	IMPVALL.H/H-E07140	6.53	0.56	0.34
3	Imperial Valley-06	1979	EI Centro Array #5	IMPVALL.H/H-E05140	6.53	3.95	0.53
4	Kobe/Japan	1995	KJMA	KOBE/KJM000	6.90	0.96	0.83
5	Kocaeli	1999	Yarimca	KOCAELI/YPT060	7.51	4.83	0.23
6	Chi-Chi	1999	TCU052	CHICHI/TCU052-E	7.62	0.66	0.36
7	Chi-Chi	1999	TCU065	CHICHI/TCU065-E	7.62	0.57	0.79
8	Duzce	1999	Duzce	DUZCE/DZC180	7.14	6.58	0.40
9	Bam/Iran	2003	Bam	BAM/BAM-L	6.60	1.70	0.81
10	Darfield	2010	GDLC	DARFIELD/GDLCN55W	7.00	1.22	0.76
11	Darfield	2010	TPLC	DARFIELD/TPLCN27W	7.00	6.11	0.30
12	Landers	1992	Lucerne	LANDERS/LCN260.AT2	7.28	2.19	0.73

increasing PGA for the three distinct ground motion sets. The regression fit equations for the examined tunnels considering different ground motion sets can be expressed as follows:

For the examined tunnels considering NFNP, Eq. (9) represents the regression fit equation as follows, where DM_{NFNP} means the damage measure for NFNP record sets.

$$\ln(DM_{NFNP}) = 1.14\ln(PGA) - 6.35 \quad (9)$$

For the examined tunnels considering NFP, Eq. (10) represents the regression fit equation as follows, where DM_{NFP} means the damage measure for NFP record sets.

$$\ln(DM_{NFP}) = 1.54\ln(PGA) - 5.58 \quad (10)$$

For the examined tunnels considering FF, Eq. (11) represents the regression fit equation as follows, where DM_{FF} means the damage measure for FF record sets.

$$\ln(DM_{FF}) = 1.40\ln(PGA) - 6.05 \quad (11)$$

For the examined tunnels considering All, Eq. (12) represents the regression fit equation as follows, where DM_{All} means the damage measure for All record sets.

$$\ln(DM_{All}) = 1.38\ln(PGA) - 5.96 \quad (12)$$

Figure 12 presents a comparison of the relationship between IM and DM of the tunnels examined in this study under three sets of ground motion records: NFNP, NFP, FF, and All. It was generally observed that the tunnel damage data increased as the PGA increased. Additionally, divergences were observed in the DM–IM relationship across the various ground motion record sets. Specifically, for low seismic intensities, the tunnel damage data DM_{NFNP} exhibited a significantly higher value than DM_{NFP} and DM_{FF}. However, as the seismic intensity gradually increased, the tunnel damage data DM_{NFP} became the highest, followed by DM_{FF} and DM_{NFNP}. This observation suggests that the divergences between the three examined ground motion record sets are influenced by the earthquake intensity level.

Furthermore, the regression fit equations, i.e., Eqs. (9)–(12), can be utilized to determine IM_{mi} based on various thresholds of damage states. The spreading of the simulated DMs concerning the regression fit gives rise to the computation of seismic demand uncertainty β_D, whereas Eq. (2) is employed to calculate the overall variability β_{tot}. Table 7 presents the fragility curves parameters, i.e., IM_{mi}, β_{DSi}, β_D and β_{tot}, of the examined tunnels, considering various ground motion sets. Consequently, the numerical fragility curves for the examined tunnels can be developed using these parameters. By using different PGA levels, the exceeding probability of tunnels reaching different damage states can be obtained correspondingly.

4.2 Generation of numerical fragility curves

Figure 13 displays the seismic fragility curves for slight/-moderate and significant damage states of the circular tunnels that were studied under different types of seismic motions: NFNP, NFP, FF records, and All. It is observed from Fig. 13 that the probability of damage gradually rises with the increase of intensity measure (represented by PGA) for every damage state and all the considered ground motion record sets. Furthermore, for the same magnitude of PGA and ground motion record set, a slightly larger damage probability for the slight/moderate damage state is observed by comparison with the extensive damage state. For instance, at a PGA of 1.0g and under FF records condition, the probability of experiencing slight/moderate damage is around 74.3%, while the probability of experiencing extensive damage is 67.2%.

Furthermore, the examination of Fig. 13(a) and (b) reveals that, among the three types of ground motion records considered, the highest probability of tunnel damage is observed under NFP for each damage state, at an equivalent PGA level. In contrast, the lowest probability of tunnel damage is observed in the instance of NFNP records. For instance, when PGA is set to 0.5g and considering the extensive damage state, the probabilities of tunnel damage are determined to be 47.1%, 86.8%, and 67.2% for NF, NFP, and FF records, respectively. It is noteworthy that

Table 5
Selected far-field ground motions.

No.	Earthquake event	Years	Station	Component	Magnitude M	Source-to-site distance R (km)	PGA (g)
1	San Fernando	1971	LA-Hollywood Stor FF	RSN68_SFERN_PEL090.AT2	6.61	22.77	0.22
2	Imperial Valley-06	1979	Delta	RSN169_IMPVALL.H_H-DLT262.AT2	6.53	22.03	0.24
3	Morgan Hill	1984	Gilroy Array #3	RSN457_MORGAN_G03090.AT2	6.19	13.01	0.20
4	Superstition Hills-02	1987	El Centro Imp. Co. Cent	RSN721_SUPER.B_B-ICC000.AT2	6.54	18.2	0.33
5	Superstition Hills-02	1987	Imperial Valley Wildlife Liquefaction Array	RSN729_SUPER.B_B-IVW090.AT2	6.54	23.85	0.20
6	Loma Prieta	1989	Anderson Dam (Downstream)	RSN739_LOMAP_AND250.AT2	6.93	20.26	0.240
7	Landers	1992	Coolwater	RSN848_LANDERS_CLW-LN.AT2	7.28	19.74	0.28
8	Landers	1992	Yermo Fire Station	RSN900_LANDERS_YER270.AT2	7.28	23.62	0.24
9	Kobe	1995	Abeno	RSN1100_KOBE_ABN090.AT2	6.90	24.85	0.23
10	Kobe	1995	Fukushima	RSN1104_KOBE_FKS090.AT2	6.90	17.85	0.21
11	Kocaeli	1999	Arcelik	RSN1148_KOCAELI_ARE000.AT2	7.51	13.49	0.20
12	Kocaeli	1999	Duzce	RSN1158_KOCAELI_DZC180.AT2	7.51	15.37	0.31
13	Chi-Chi	1999	CHY101	RSN1244_CHICHI_CHY101-E.AT2	7.62	9.94	0.31
14	Duzce	1999	Bolu	RSN1602_DUZCE_BOL000.AT2	7.14	12.04	0.74
15	Trinidad	1980	Rio Dell Overpass_E Ground	RSN281_TRINIDAD.B_B-RDE000.AT2	7.20	76.06	0.16
16	Manjil_Iran	1990	Abhar	RSN1634_MANJIL_184057.AT2	7.37	75.58	0.12
17	Chi-Chi	1999	TCU088	RSN1520_CHICHI_TCU088-N.AT2	7.62	18.16	0.43
18	Niigata_Japan	2004	NIG023	RSN4213_NIIGATA_NIG023NS.AT2	6.63	25.82	0.27
19	Chuetsu-oki	2007	Kashiwazaki City Center	RSN4856_CHUETSU_65025NS.AT2	6.80	11.09	0.45
20	Chuetsu-oki	2007	Kashiwazaki City Takayanagicho	RSN4873_CHUETSU_65056NS.AT2	6.80	20.03	0.73
21	Chuetsu-oki	2007	Oguni Nagaoka	RSN4874_CHUETSU_65057NS.AT2	6.80	20.00	0.61
22	Superstition Hills-02	1987	Plaster City	RSN724_SUPER.B_B-PLS045.AT2	6.54	22.25	0.14
23	Kocaeli_Turkey	1999	Atakoy	RSN1149_KOCAELI_ATK000.AT2	7.51	58.28	0.11
24	Kocaeli_Turkey	1999	Cekmece	RSN1157_KOCAELI_CNA000.AT2	7.51	66.69	0.18

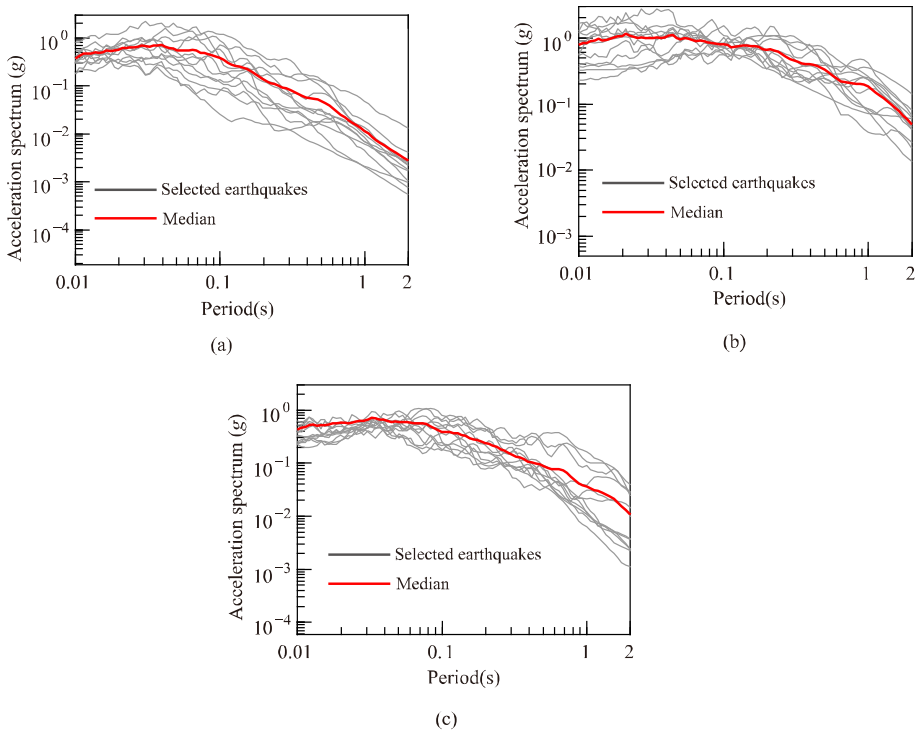

Fig. 8. Acceleration spectrum of selected earthquake records at the ground surface (damping ratio: 5%). (a) NFNP, (b) NFP, and (c) FF.

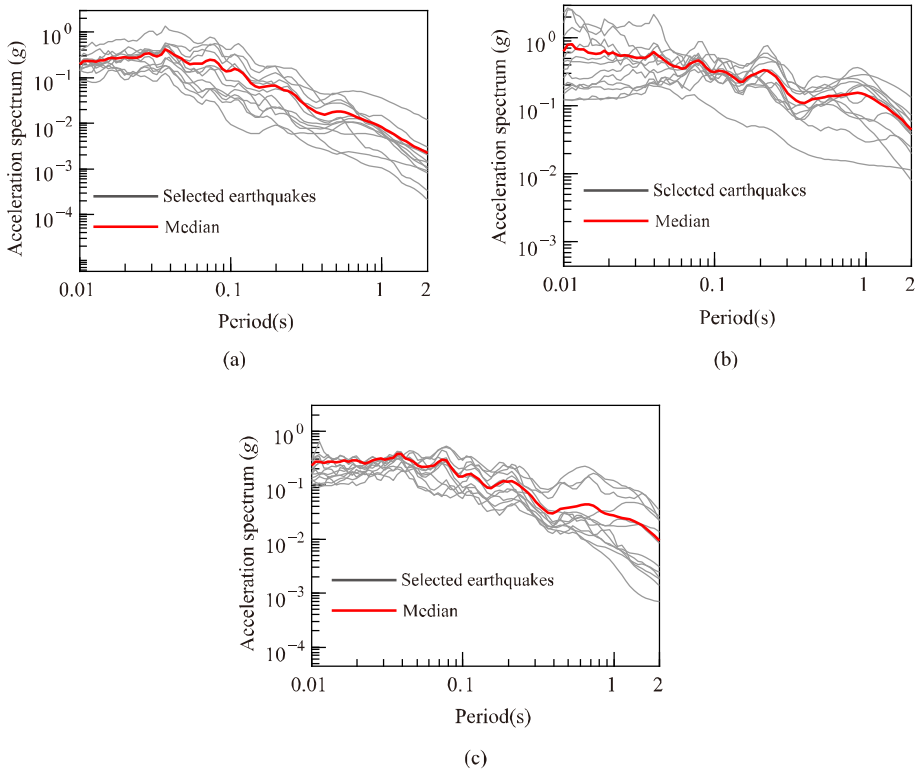

Fig. 9. Deconvolved acceleration spectrum of selected earthquake records at engineering bedrock (damping ratio: 5%). (a) NFNP, (b) NFP, and (c) FF.

the probability of tunnel damage for NFP records is nearly twice as high as that for NFNP records. Moreover, the investigation indicates that the highest probabilities of damage occur in the case of NFP records. These probabilities are recorded as 19.2% at 0.4*g*, 78.6% at 0.8*g*, and 96.1% at 1.2*g* for slight/moderate damage (Fig. 13(a)), and as 15.2% at 0.4*g*, 72.4% at 0.8*g*, and 93.8% at 1.2*g* for extensive damage (Fig. 13(b)). Consequently, it can be concluded from this

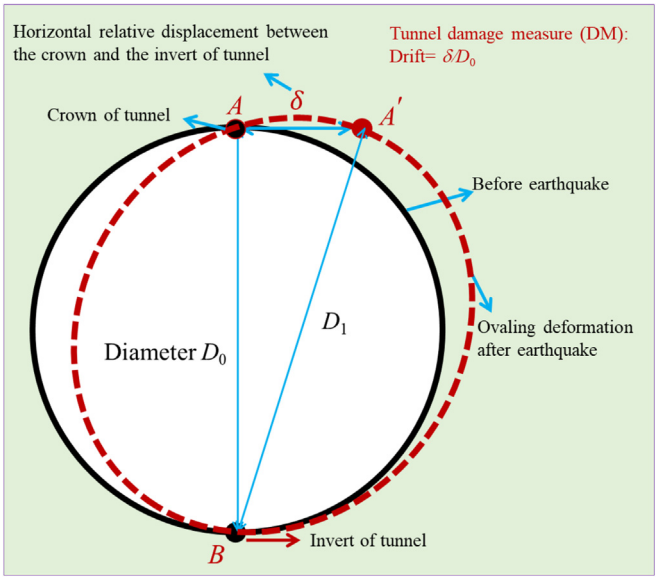

Fig. 10. Definition of DM of tunnel lining under seismic loading (Andreotti & Lai, 2019).

study that when the tunnel is exposed to NFNP, it exhibits a higher vulnerability or susceptibility to collapse at high intensity levels. As demonstrated by the comparative results, these several types of earthquake frequency components result in a notable discrepancy in the seismic vulnerability of the examined shield tunnel.

4.3 Comparisons with existing empirical fragility curves

The proposed fragility curves within this work under various ground motion sets were further compared with the existing empirical curves proposed by ALA (2001), as depicted in Fig. 14. As past earthquakes lack extensive damage data, only the minor and moderate damage states were compared. Figure 14 clearly illustrates that the developed analytical fragility curves under different ground motion sets significantly differ from the empirical ones, and this can be explained by three factors. Firstly, the characteristics of the soil-tunnel system studied in this work differ from those examined by ALA (2001), which includes different geological conditions, tunnel dimensions, and burial depths, among other factors. Secondly, the empirical tunnel damage database utilized by ALA (2001) was not categorized according to different ground motion record sets due to the lack of detailed earthquake data, leading to a failure to account for how the fragility curve is affected by the ground motion characteristics. Moreover, the fragility functions established in this work only account for the influence of shear waves. However, the empirical ones generated by ALA (2001) integrate the effects of various practical earthquake factors, encompassing both shear waves and P-waves. The above discussion may also constitute a significant factor contributing to the notable disparities observed in the comparison between the two approaches. In conclusion, the comparisons made with the empirical fragility curves serve to underscore the crucial importance of ground motion characteristics in the formation of fragility curves.

5 Conclusions

This work examined the impact of earthquake characteristics on the fragility of the shield tunnels. To achieve this, the seismic fragility curves of the examined tunnels were generated considering different ground motion sets, including NFNP, NFP, and FF. The examined soil-tunnel system was simulated using ABAQUS platform, and the tunnel seismic response was derived using a large number of nonlinear dynamic numerical analysis. The tunnel drift and the PGA was defined as the DM and the IM in this study, respectively. A two-parameter fragility model with the logarithm of the mean IM value IM_{mi} and the standard deviation β_{tot} was then proposed to characterize the seismic vulnerability of the examined tunnels. Fragility curves were then developed for the examined tunnel subjected to NFNP, NFP, and FF. It is identified that the damage probability for each tunnel damage state by NFP is the highest among the three categories of ground motion records considered. The comparisons with empirical fragility curves also highlighted the critical importance of ground motion characteristics in the formation of fragility curves. By adopting the developed fragility curves, the damage probability for the similar tunnel structures can be qualitatively evaluated. The findings of this study can also enhance the reliability of seismic risk and resilience assessment of tunnels, as they directly consider the influence of different ground motions characteristics and soil-structure interaction.

Future research should take into account various soil-tunnel system configurations, seismic demand factors, and various ground motion intensity measures for more precise seismic vulnerability assessment outcomes. Moreover, the current investigation specifically addresses the uncertainties associated with ground motions in the seismic

Table 6
Definition of performance level of the examined circular tunnels (Andreotti & Lai, 2019).

Damage states (D_S)	Damage measure (DM)		Damage description
	Drift (δ/D_0)	Log std	
No damage: $D_{S,0}$	–	–	No damage detectable by visual inspection
Slight/moderate damage: $D_{S,1}$	$\delta/D_0 = 0.16\%$	$\beta_{DS1} = 0.22$	Damage detectable by visual inspection Potential cracking, spalling and water leakage
Extensive damage: $D_{S,2}$	$\delta/D_0 = 0.18\%$	$\beta_{DS2} = 0.24$	Large cracking, spalling, uplift and water leakage

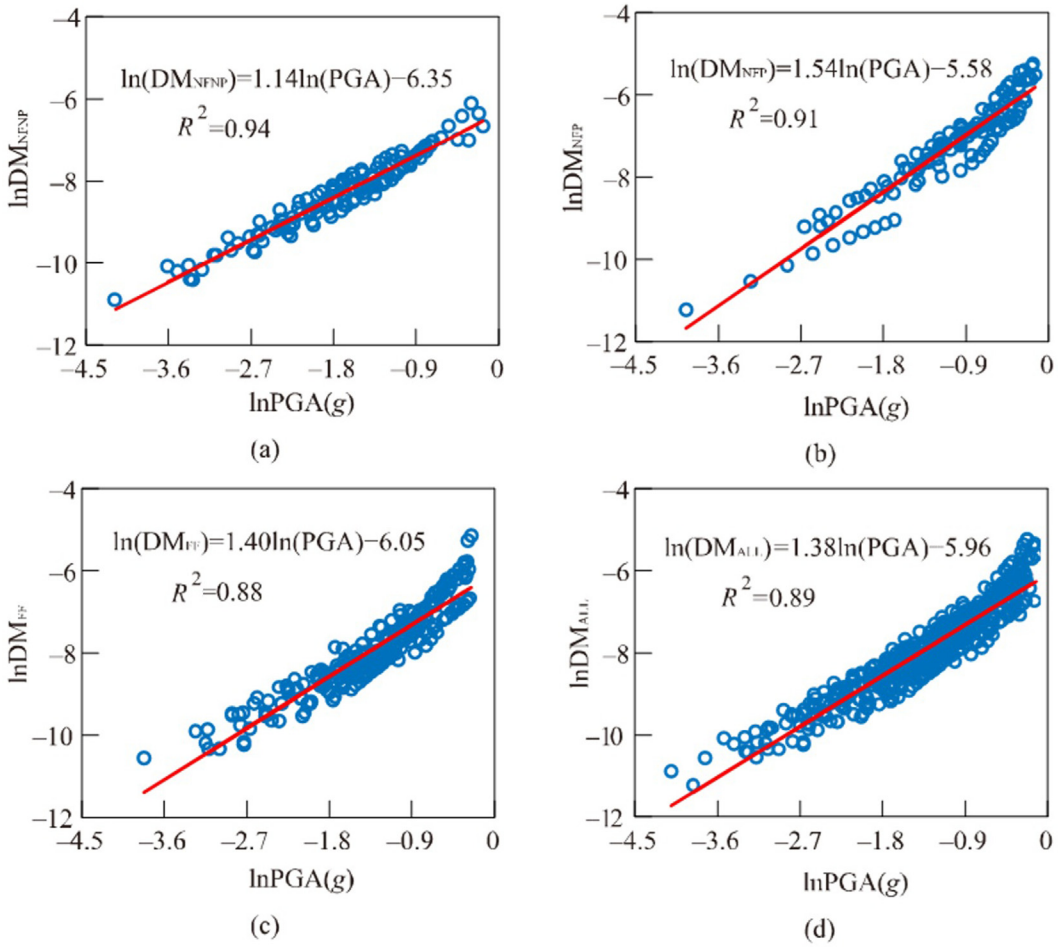

Fig. 11. DM versus IM for various ground motion record sets, including (a) NFNP, (b) NFP, (c) FF, and (d) All.

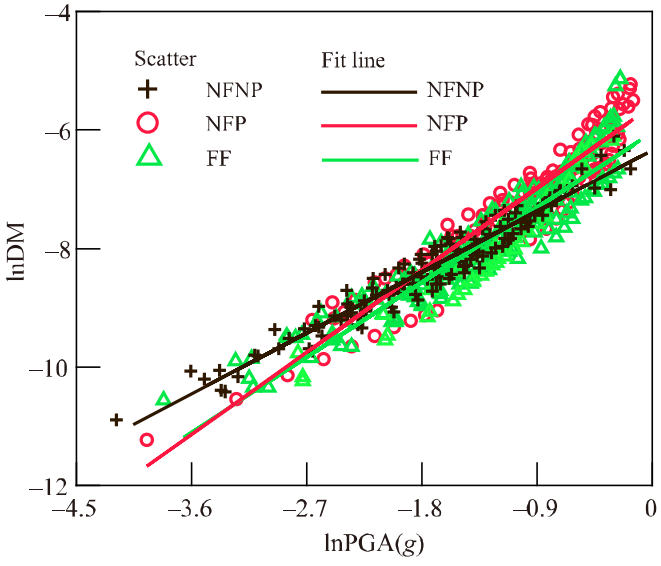

Fig. 12. Comparisons of DM–IM relationship for various ground motion records: NFNP, NFP, FF, and All.

response assessment of tunnels. Future studies could extend their scope to encompass the stochastic nature of both loads and resistances, as discussed in works by Zhang and Liu (2020) and Feng et al. (2023). This would involve examining uncertainties arising from soil parameters and structural properties of tunnel structures, contributing to a more comprehensive and accurate assessment of seismic fragility. Although the PGA was used as the IM in this study, the optimal IMs for different types of ground motion sets may vary. An optimal IM should accurately indicate the frequency content, amplitude, and duration of ground motions in order to reduce the variability of seismic structure performance. In this regard, our future research will concentrate on extracting the optimal IM for various ground motion sets.

Furthermore, it is noted that the P-waves can alter the stress distribution within the tunnel structure, and contribute to the dynamic loading of tunnels during an earthquake (Chen & Yu, 2023). The compressive forces exerted by P-waves may interact with the tunnel lining, influencing the structural response and potentially leading to different failure modes compared to shear waves. This study only on the effects

Table 7
Derived fragility curves parameters of the examined tunnels.

Tunnels under various ground motion record sets	Damage states	Median IM_{mi} (g)	Standard deviation		
			β_{DSi}	β_D	β_{tot}
NFNP	$D_{S,1}$: Slight/Moderate	0.924	0.22	0.227	0.316
	$D_{S,2}$: Extensive	1.024	0.24	0.227	0.330
NFP	$D_{S,1}$: Slight/Moderate	0.575	0.22	0.354	0.417
	$D_{S,2}$: Extensive	0.621	0.24	0.354	0.428
FF	$D_{S,1}$: Slight/Moderate	0.757	0.22	0.367	0.428
	$D_{S,2}$: Extensive	0.823	0.24	0.367	0.438
All	$D_{S,1}$: Slight/Moderate	0.709	0.22	0.373	0.433
	$D_{S,2}$: Extensive	0.773	0.24	0.373	0.444

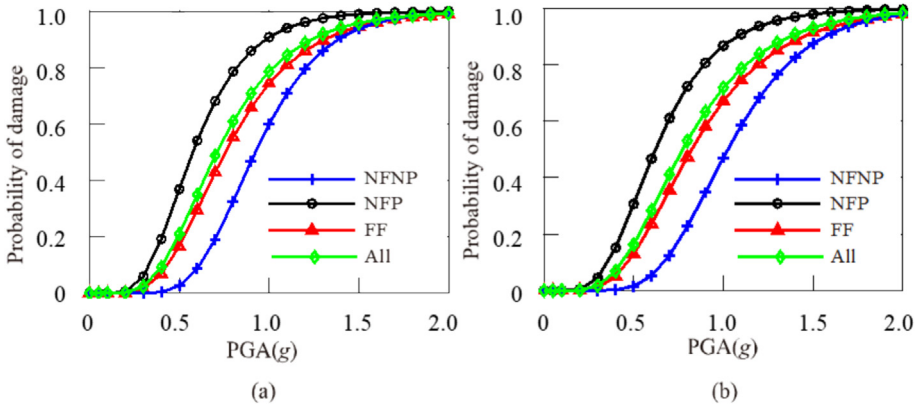

Fig. 13. Derived fragility functions under different ground motions sets. (a) Slight/moderate, and (b) extensive.

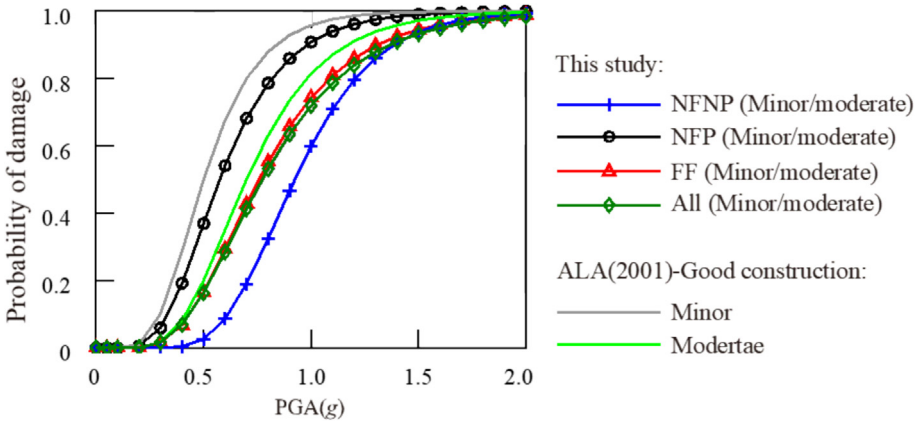

Fig. 14. Comparison of developed fragility curves and empirical ones of ALA (2001).

of vertically propagating shear waves, further investigations will be conducted to assess the effects of P-waves and shear waves on the seismic fragility assessment of tunnels.

Data availability

The data that support the findings of this study are available from the corresponding author upon reasonable request.

CRediT authorship contribution statement

Zhong-Kai Huang: Writing – review & editing, Data curation, Writing – original draft, Formal analysis, Conceptualization, Methodology. **Dong-Mei Zhang:** Conceptualization, Writing – review & editing, Supervision. **Wu-Yu Zhang:** Methodology, Resources, Conceptualization. **Yong-Bo Li:** Project administration, Resources, Data curation.

Declaration of competing interest

The authors declare that they have no known competing financial interests or personal relationships that could have appeared to influence the work reported in this paper.

Acknowledgement

The authors appreciate the support from the National Key Research and Development Program of China (Grant Nos. 2022YFC3800905 and 2021YFF0502200), National Natural Science Foundation of China (Grant Nos. 52478410, 52090082, and 52238010), Young Elite Scientists Sponsorship Program by CAST (2023QNRC001), and Fundamental Research Program of the Qinghai Science and Technology Department (2023-ZJ-926M).

References

ABAQUS, A. (2012). *Theory and analysis user's manual, version 6.12*. Providence, RI, USA: Dassault Systèmes SIMULIA.

Al-Janabi, H. A., & Aubeny, C. P. (2022). Experimental and numerical investigation of the performance of piles and suction caissons subjected to inclined cyclic loading in cohesive soils. *Journal of Geotechnical and Geoenvironmental Engineering, 148*(6), 04022036.

American Lifelines Alliance (2001). *Seismic fragility formulations for water systems: Guideline*. Washington, DC: American Lifelines Alliance.

Anastasopoulos, I., Gelagoti, F., Kourkoulis, R., & Gazetas, G. (2011). Simplified constitutive model for simulation of cyclic response of shallow foundations: Validation against laboratory tests. *Journal of Geotechnical and Geoenvironmental Engineering, 137*(12), 1154–1168.

Anastasopoulos, I., Georgarakos, T., Georgiannou, V., Drosos, V., & Kourkoulis, R. (2010). Seismic performance of bar-mat reinforced-soil retaining wall: Shaking table testing versus numerical analysis with modified kinematic hardening constitutive model. *Soil Dynamics and Earthquake Engineering, 30*(10), 1089–1105.

Andreotti, G., & Lai, C. G. (2019). Use of fragility curves to assess the seismic vulnerability in the risk analysis of mountain tunnels. *Tunnelling and Underground Space Technology, 91*, 103008.

Ansari, A., Rao, K. S., & Jain, A. K. (2023). Seismic response and fragility evaluation of circular tunnels in the Himalayan region: Implications for post-seismic performance of transportation infrastructure projects in Jammu and Kashmir. *Tunnelling and Underground Space Technology, 137*, 105118.

Antoniou, M., Mantakas, A., Nikitas, N., & Fuentes, R. (2023). A numerical case study on the long-term seismic assessment of reinforced concrete tunnels in corrosive environments. *Journal of Rock Mechanics and Geotechnical Engineering, 15*(3), 551–572.

Argyroudis, S. A., & Pitilakis, K. D. (2012). Seismic fragility curves of shallow tunnels in alluvial deposits. *Soil Dynamics and Earthquake Engineering, 35*, 1–12.

Argyroudis, S., Tsinidis, G., Gatti, F., & Pitilakis, K. (2017). Effects of SSI and lining corrosion on the seismic vulnerability of shallow circular tunnels. *Soil Dynamics and Earthquake Engineering, 98*, 244–256.

Asakura, T., & Sato, Y. (1996). Damage to mountain tunnels in hazard area. *Soils and Foundations, 36*, 301–310.

Bilotta, E., Lanzano, G., Madabhushi, S. G., & Silvestri, F. (2014). A numerical Round Robin on tunnels under seismic actions. *Acta geotechnicaGeotechnica, 9*(4), 563–579.

Chen, X., Shen, J., Bao, X., Wu, X., Tang, W., & Cui, H. (2023). A review of seismic resilience of shield tunnels. *Tunnelling and Underground Space Technology, 136*, 105075.

de Silva, F., Fabozzi, S., Nikitas, N., Bilotta, E., & Fuentes, R. (2021). Seismic vulnerability of circular tunnels in sand. *Géotechnique, 71*(11), 1056–1070.

Dowding, C. H., & Rozan, A. (1978). Damage to rock tunnels from earthquake shaking. *Journal of the Geotechnical Engineering Division, 104*(2), 175–191.

El Ganainy, H., & El Naggar, M. H. (2009). Seismic performance of three-dimensional frame structures with underground stories. *Soil Dynamics and Earthquake Engineering, 29*(9), 1249–1261.

Fabozzi, S., Bilotta, E., & Lanzano, G. (2017). A numerical study on seismic vulnerability of tunnel linings. In *Proceedings of 3rd performance based design in earthquake geotechnical engineering. Vancouver, Canada* (pp. 16–19).

Feng, S., Dai, S., & Lei, H. (2023). Application of an integrated nonuniform seismic random excitation method in tunnel engineering in soft soil areas. *Computers and Geotechnics, 153*, 105043.

Hashash, Y. M. A., Musgrove, M. I., & Harmon, J. A. (2018). Nonlinear and equivalent linear seismic site response of one-dimensional soil columns. *User Manual v7. 0, Deepsoil Software, 12*(10).

Hashash, Y. M., Hook, J. J., Schmidt, B., John, I., & Yao, C. (2001). Seismic design and analysis of underground structures. *Tunnelling and Underground Space Technology, 16*(4), 247–293.

Hashash, Y. M., Park, D., John, I., & Yao, C. (2005). Ovaling deformations of circular tunnels under seismic loading, an update on seismic design and analysis of underground structures. *Tunnelling and Underground Space Technology, 20*(5), 435–441.

He, Z., & Chen, Q. (2019). Vertical seismic effect on the seismic fragility of large-space underground structures. *Advances in Civil Engineering, 2019*(1), 1–17, 96502942019.

Hu, X., Zhou, Z., Chen, H., & Ren, Y. (2020). Seismic fragility analysis of tunnels with different buried depths in a soft soil. *Sustainability, 12*(3), 892.

Huang, G., Qiu, W., & Zhang, J. (2017). Modelling seismic fragility of a rock mountain tunnel based on support vector machine. *Soil Dynamics and Earthquake Engineering, 102*, 160–171.

Huang, P., & Chen, Z. (2022). Fragility analysis for subway station using artificial neural network. *Journal of Earthquake Engineering, 26*(13), 6724–6744.

Huang, Z. K., & Zhang, D. M. (2021). Scalar-and vector-valued vulnerability analysis of shallow circular tunnel in soft soil. *Transportation Geotechnics, 27*, 100505.

Huang, Z., Zeng, N., Zhang, D., Argyroudis, S., & Mitoulis, S. (2025). Resilience Models for Tunnels Recovery After Earthquakes. *Engineering*.

Huang, Z. K., Pitilakis, K., Argyroudis, S., Tsinidis, G., & Zhang, D. M. (2021). Selection of optimal intensity measures for fragility assessment of circular tunnels in soft soil deposits. *Soil Dynamics and Earthquake Engineering, 145*, 106724.

Huang, Z., Argyroudis, S., Zhang, D., Pitilakis, K., Huang, H., & Zhang, D. (2022). Time-dependent fragility functions for circular tunnels in soft soils. *ASCE-ASME Journal of Risk and Uncertainty in Engineering Systems, Part A: Civil Engineering, 8*(3), 04022030.

Ishibashi, I., & Zhang, X. (1993). Unified dynamic shear moduli and damping ratios of sand and clay. *Soils and Foundations, 33*(1), 182–191.

Jalayer, F., & Cornell, C. A. (2009). Alternative non-linear demand estimation methods for probability-based seismic assessments. *Earthquake Engineering & Structural Dynamics, 38*(8), 951–972.

Jiang, J., El Naggar, M. H., Huang, W., Xu, C., Zhao, K., & Du, X. (2022). Seismic vulnerability analysis for shallow-buried underground frame structure considering 18 existing subway stations. *Soil Dynamics and Earthquake Engineering, 162*, 107479.

Kanellopoulos, K., & Gazetas, G. (2020). Vertical static and dynamic pile-to-pile interaction in non-linear soil. *Géotechnique, 70*(5), 432–447.

Kassem, M. M., Nazri, F. M., & Farsangi, E. N. (2020). The seismic vulnerability assessment methodologies: A state-of-the-art review. *Ain Shams Engineering Journal, 11*(4), 849–864.

Kazemi, F., Asgarkhani, N., & Jankowski, R. (2023). Machine learning-based seismic fragility and seismic vulnerability assessment of reinforced concrete structures. *Soil Dynamics and Earthquake Engineering, 166*, 107761.

Kontoe, S., Zdravkovic, L., Potts, D. M., & Menkiti, C. O. (2008). Case study on seismic tunnel response. *Canadian Geotechnical Journal, 45*(12), 1743–1764.

Lee, J., & Fenves, G. L. (1998). Plastic-damage model for cyclic loading of concrete structures. *Journal of Engineering Mechanics, 124*(8), 892–900.

Li, T. (2012). Damage to mountain tunnels related to the Wenchuan earthquake and some suggestions for aseismic tunnel construction. *Bulletin of Engineering Geology and the Environment, 71*(2), 297–308.

Li, Y., Wang, R., Ma, H., & Zhang, J. M. (2025). Rising groundwater table due to restoration projects amplifies earthquake induced liquefaction risk in Beijing. *Nature Communications, 16*(2025), 1466.

Liu, H., Song, K., Ye, Z., Wang, C., & Liu, H. (2022). Seismic fragility analysis of in-service shield tunnels considering surface building and joint-bolt corrosion. *Soil Dynamics and Earthquake Engineering, 162*, 107455.

Lou, M. L., & Shao, X. G. (2013). Discussion on modeling issues of Rayleigh damping matrix in soil layers with deep deposit. *Chinese Journal of Geotechnical Engineering, 35*(7), 1272–1279 (in Chinese).

Lysmer, J., & Kuhlemeyer, R. L. (1969). Finite dynamic model for infinite media. *Journal of the Engineering Mechanics Division, 95*(4), 859–877.

Moschonas, I. F., Kappos, A. J., Panetsos, P., Papadopoulos, V., Makarios, T., & Thanopoulos, P. (2009). Seismic fragility curves for Greek bridges: Methodology and case studies. *Bulletin of Earthquake Engineering, 7*(2), 439–468.

Nielson, B. G., & DesRoches, R. (2007). Seismic fragility methodology for highway bridges using a component level approach. *Earthquake Engineering & Structural Dynamics, 36*(6), 823–839.

Omranian, E., Abdelnaby, A. E., & Abdollahzadeh, G. (2018). Seismic vulnerability assessment of RC skew bridges subjected to mainshock-aftershock sequences. *Soil Dynamics and Earthquake Engineering, 114*, 186–197.

Design of structures for earthquake resistance. (2004). Brussels, Belgium: European Committee for Standardisation.

Pacific Earthquake Engineering Research Center. (2000) Pacific Earthquake Engineering Research Strong Motion Database. https://ngawest2.berkeley.edu/.

Patil, M., Choudhury, D., Ranjith, P. G., & Zhao, J. (2018). Behavior of shallow tunnel in soft soil under seismic conditions. *Tunnelling and Underground Space Technology, 82*, 30–38.

Qiu, W., Huang, G., Zhou, H., & Xu, W. (2018). Seismic vulnerability analysis of rock mountain tunnel. *International Journal of Geomechanics, 18*(3), 04018002.

Shome, N., Cornell, C. A., Bazzurro, P., & Carballo, J. E. (1998). Earthquakes, records, and nonlinear responses. *Earthquake Spectra, 14*(3), 469–500.

Sun, B., Deng, M., Zhang, S., Cui, W., Wang, C., Yu, L., & Cao, K. (2020). Inelastic dynamic analysis and damage assessment of a hydraulic arched tunnel under near-fault SV waves with arbitrary incoming angles. *Tunnelling and Underground Space Technology, 104*, 103523.

Tsinidis, G. (2018). Response of urban single and twin circular tunnels subjected to transversal ground seismic shaking. *Tunnelling and Underground Space Technology, 76*, 177–193.

Tsinidis, G., Karatzetzou, A., & Stefanidou, S. (2024). On the effects of salient parameters for an efficient assessment of seismic response and fragility of circular tunnels in clayey deposits. *Soil Dynamics and Earthquake Engineering, 178*, 108490.

Tsinidis, G., Karatzetzou, A., Stefanidou, S., & Markogiannaki, O. (2022). Developments in seismic vulnerability assessment of tunnels and underground structures. *Geotechnics, 2*(1), 209–249.

Vamvatsikos, D., & Cornell, C. A. (2002). Incremental dynamic analysis. *Earthquake Engineering & Structural Dynamics, 31*(3), 491–514.

Wang, L., Geng, P., Chen, J., & Wang, T. (2023). Machine learning-based fragility analysis of tunnel structure under different impulsive seismic actions. *Tunnelling and Underground Space Technology, 133*, 104953.

Wu, W., Ge, S., Yuan, Y., Ding, W., & Anastasopoulos, I. (2020). Seismic response of subway station in soft soil: Shaking table testing versus numerical analysis. *Tunnelling and Underground Space Technology, 100*, 103389.

Zhang, L., & Liu, Y. (2020). Numerical investigations on the seismic response of a subway tunnel embedded in spatially random clays. *Underground Space, 5*(1), 43–52.

Zhong, Z., Feng, L., Shen, J., & Du, X. (2024). Seismic fragility analysis of subway station structure subjected to sequence-type ground motions. *Tunnelling and Underground Space Technology, 144*, 105570.

Zhong, Z., Ni, B., Shi, Y., Shen, J., & Du, X. (2023). Convolutional neural network-based seismic fragility analysis of subway station structure considering spatial variation of site shear-wave velocity. *Computers and Geotechnics, 163*, 105741.

Zi, H., Ding, Z., Ji, X., Liu, Z., & Shi, C. (2021). Effect of voids on the seismic vulnerability of mountain tunnels. *Soil Dynamics and Earthquake Engineering, 148*, 106833.